mater.scichina.com link.springer.com

Fast and stable Mg^{2+} intercalation in a high voltage $NaV_2O_2(PO_4)_2F$/rGO cathode material for magnesium-ion batteries

Junjun Wang[1†], Shuangshuang Tan[1†], Guobin Zhang[1], Yalong Jiang[1], Yameng Yin[1], Fangyu Xiong[1], Qidong Li[1], Dan Huang[1], Qinghua Zhang[2], Lin Gu[2], Qinyou An[1*] and Liqiang Mai[1*]

ABSTRACT Sluggish kinetics of Mg^{2+} intercalation and low working potential seriously hinder the development of high-energy-density magnesium-ion batteries (MIBs). Hence developing cathode materials with fast Mg^{2+} diffusion and high working voltage is a key to overcome the obstacles in MIBs. Herein, a tetragonal $NaV_2O_2(PO_4)_2F$/reduced graphene oxide (rGO) is proposed as an effective Mg^{2+} host for the first time. It exhibits the highest average discharge voltage (3.3 V *vs.* Mg^{2+}/Mg), fast diffusion kinetics of Mg^{2+} with the average diffusivity of 2.99×10^{-10} cm^2 s^{-1}, and ultralong cycling stability (up to 9500 cycles). The Mg^{2+} storage mechanism of $NaV_2O_2(PO_4)_2F$/rGO is demonstrated as a single-phase (de) intercalation reaction by *in situ* X-ray diffraction (XRD) technology. Density functional theory (DFT) computations further reveal that Mg^{2+} ions tend to migrate along the *a* direction. X-ray absorption near edge structure (XANES) demonstrates a decrease in the average valence of vanadium, and the local coordination environment around vanadium site is highly conserved after magnesiation. Moreover, the assembled $NaV_2O_2(PO_4)_2F//Mg_{0.79}NaTi_2(PO_4)_3$ Mg-ion full cell exhibits high power and energy densities, which indicates that $NaV_2O_2(PO_4)_2F$/rGO owns potential for practical applications. This work achieves a breakthrough in the working voltage of cathode materials for MIBs and provides a new opportunity for high-energy-density MIBs.

Keywords: high-voltage, fast kinetics, MIBs, fluorophosphate, full cell

INTRODUCTION

Magnesium-ion batteries (MIBs) are considered as a potential candidate for large-scale energy storage system owing to abundant sources (2% of the total mass of the earth's crust) [1], low redox potential (−2.37 V *vs.* standard hydrogen electrode (SHE)), high safety [2–4] and high volumetric capacity (3833 mA h cm^{-3}) of Mg metal anode. In 2000, Aurbach *et al.* [5] displayed the first MIB prototype based on the Chevrel phase Mo_6S_8 cathode material. There is no doubt that this material has made many excellent breakthroughs in the past decades; however, the low working voltage (~1.1 V *vs.* Mg^{2+}/Mg) and limited discharge capacity (~90 mA h g^{-1}) hinder its further development. Since then, some new cathode materials [6–24] have been gradually developed. Unfortunately, most of them still show low discharge voltages, such as V_2O_5 (~1.35 V) [6], $VOPO_4$ (~1.0 V) [12], MnO_2 (~1.5 V) [7], $H_2V_3O_8$ (~2.0 V) [10] and almost all layered transition metal chalcogenides (~1.0 V) [8,9,11,25]. Therefore, the development of cathode materials with high working voltage is of great significance for high-energy-density MIBs.

In recent years, researchers have put a lot of efforts to develop high-voltage cathode materials for MIBs and have made some progress. For instance, Huang's group [14] reported that $V_2(PO_4)_3$ exhibited a high discharge voltage (~2.9 V) with 5 cycles at 9.85 mA g^{-1} and 55°C. Honma's group and Cabana's group reported that Mn_2O_4 [26] and $MgCoSiO_4$ [27] presented the working voltage of ~2.6 V, and their cycle life is less than 30 cycles. To the best of our knowledge, Cui's group [28] reported that NiHCF had the highest working voltage (~3.0 V) with the discharge capacity of 52 mA h g^{-1} at 10 mA g^{-1} till now. Obviously, the high-voltage cathode materials mentioned above still have large room for improvement in some

---

[1] State Key Laboratory of Advanced Technology for Materials Synthesis and Processing, Wuhan University of Technology, Wuhan 430070, China
[2] Institute of Physics, Chinese Academy of Sciences, Beijing 100190, China

[†] These authors contributed equally to this work.

[*] Corresponding authors (emails: anqinyou86@whut.edu.cn (An Q); mlq518@whut.edu.cn (Mai L))

respects, such as poor rate performance, low specific capacity and poor cyclic stability. Generally, if MIBs are to compete with lithium-ion batteries (LIBs), the working voltage should be higher than 3 V and the capacity needs to exceed 100 mA h g^{-1}. For these reasons, developing the high-voltage cathode materials with fast Mg^{2+} diffusion and enhanced electrochemical performances for MIBs at ambient temperature is significant but full of challenges.

In this study, we present a tetragonal $NaV_2O_2(PO_4)_2F$/reduced graphene oxide (rGO) obtained by a electrochemical desodiated method. When evaluated as cathode material in magnesium bis(trifluoromethylsulfonyl) imide/acetonitrile ($Mg(TFSI)_2$/AN) electrolyte, $NaV_2O_2(PO_4)_2F$/rGO shows the highest average working voltage of 3.3 V *vs.* Mg^{2+}/Mg and fast kinetics of Mg^{2+} intercalation with the average diffusion coefficient of 2.99×10^{-10} cm^2 s^{-1}. It also presents outstanding rate performance (30.3 mA h g^{-1} at 5 A g^{-1}) and ultralong cycling stability (up to 9500 cycles at 0.5 A g^{-1}). Moreover, based on the high-rate and stable $Mg_{0.79}NaTi_2(PO_4)_3$/C anode material, the assembled Mg-ion full cell delivers high energy and power densities. The reversible (de)magnetization mechanism of $NaV_2O_2(PO_4)_2F$/rGO was studied by *in situ* X-ray diffraction (XRD), X-ray absorption near-edge structure (XANES) and *ex situ* X-ray photoelectron spectroscopy (XPS) technologies.

EXPERIMENTAL SECTION

Materials synthesis

$Na_3V_2O_2(PO_4)_2F$/rGO (NVOPF/rGO) microspheres were obtained by using a spray drying and annealing procedure in the light of our previously reported method [29]. Firstly, 8 mmol NH_4VO_3, 12 mmol NaF and 8 mmol $NH_4H_2PO_4$ with a molar ratio of 1:1.5:1 were added to 200 mL ultra-pure water and then 80 mL graphene oxide (GO) solution (2 mg mL^{-1}) was poured into the above solution. Afterwards, the precursor of NVOPF/GO was prepared by a spray-drying for the mixed solution. Finally, NVOPF/rGO microspheres were prepared after calcination at 500°C in the Ar atmosphere with a heating rate of 2°C min^{-1} for 5 h and NVOPF was obtained by calcination at 400°C in the Ar atmosphere with a heating rate of 5°C min^{-1} for 5 h. The GO solution (2 mg mL^{-1}) is purchased from XFNANO Company.

The $NaTi_2(PO_4)_3$/C (NTP/C) flowers were synthesized by hydrothermal reaction and calcination [30]. Firstly, 2 mmol tetrabutyl titanate and 20 mL ethylene glycol were mixed for 20 min. Then 1 mmol glucose, 1 mmol $NaH_2PO_4\cdot2H_2O$, 2 mmol H_3PO_4 and 20 mL ultra-pure water were added to the above solution. The precursor of NTP/C was obtained by hydrothermal reaction at 180°C for 12 h and then dring the solution at 120°C. Finally, NTP/C was prepared by calcinating the precursor at 350°C for 2 h followed by 700°C for 4 h in the Ar atmosphere.

Material characterization

XRD measurement was performed using a Bruker AXS D8 Advance powder X-ray diffractometer with an area detector using Cu Kα X-ray source. Scanning electron microscopy (SEM) images were acquired by using a JEOL-7100F microscope. A Titan G2 60-300 instrument was used for transmission electron microscopy (TEM), high resolution TEM, high-angle annular dark-field (HAADF) images and energy dispersive X-ray spectroscopy (EDX) mapping tests. VG Multi Lab 2000 instrument was used for XPS measurement. Renishaw INVIA micro-Raman spectroscopy system was used for Raman experiments. XANES experiments were performed at the beamline 1W1B of Beijing Synchrotron Radiation Facility (BSRF). Energy calibration was carried out by the first derivative point of the spectrum of V foil. The XANES and extended X-ray absorption fine structure (EXAFS) data were processed by using the software packages Athena. The carbon content analyses were carried out by CHNSO elemental analyzer (Vario EL cube).

Computational details

All calculations on $NaV_2O_2(PO_4)_2F$/rGO were executed by the projector augmented wave (PAW) [31] method within density functional theory (DFT), conducted in the Vienna *ab initio* Simulation Package (VASP) [32,33]. The generalized gradient approximation (GGA) in the form of the Perdew-Burke-Ernzerhof (PBE) [34] was used to treat the exchange-correlation energy. Firstly, based on the results of Rietveld refinement results (Fig. 1b) and DFT calculations in a unit cell (2 Na, 4 V, 4 P, 2 F and 20 O) (Fig. S1) [35], the most stable crystal structure of $NaV_2O_2(PO_4)_2F$/rGO (Fig. S1a) was obtained. Then, the Mg^{2+} migration pathway in $NaV_2O_2(PO_4)_2F$/rGO and energy barrier were optimized with nudged elastic band (NEB) method in a 2×2×1 supercell containing 4 formula units (8 Na, 16 V,16 P, 8 F and 80 O). Based on previous work [36,37], two possible diffusion pathways denoted as Path 1 (perpendicular to the *ab* plane) and Path 2 (parallel to the *ab* plane) were considered (Fig. S2). A kinetic energy cutoff of 500 eV was used for wave functions expanded in the plane wave basis. Besides, spin polarization was considered. Allow all atoms to relax, if the forces

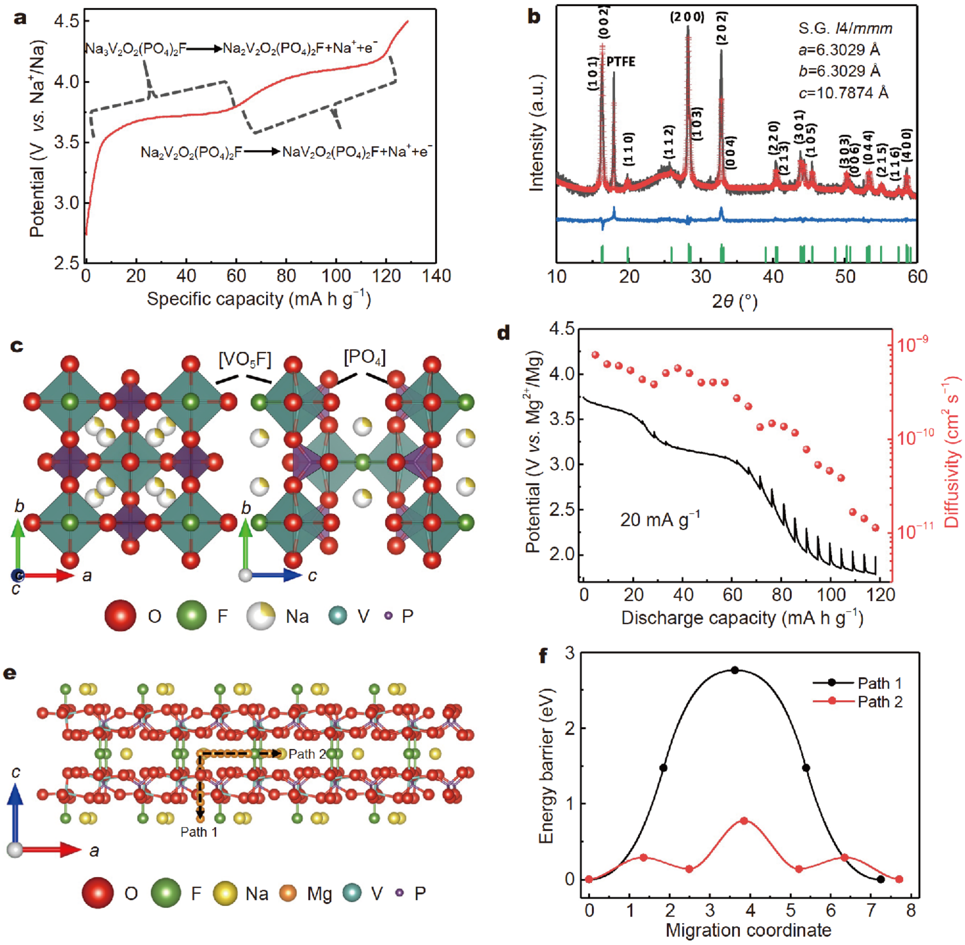

Figure 1 Crystal structure of $NaV_2O_2(PO_4)_2F$/rGO and kinetics analysis. (a) Electrochemical desodiation process of the NVOPF/rGO. (b) Rietveld refinement of $NaV_2O_2(PO_4)_2F$/rGO. The black continuous line, red crosses and blue line represent the observed, calculated and difference patterns, respectively. Vertical green tick bars mark the Bragg reflections. (c) Crystal structure of $NaV_2O_2(PO_4)_2F$/rGO: the layers in the *ab* plane (left) and in the *bc* plane (right). (d) GITT curve of the $NaV_2O_2(PO_4)_2F$/rGO electrode and diffusivity *versus* state of discharge. (e) Diffusion paths profiles of Mg^{2+} transport in $NaV_2O_2(PO_4)_2F$/rGO. (f) Diffusion energy barrier profiles of Mg^{2+} transport in $NaV_2O_2(PO_4)_2F$/rGO.

were less than 0.05 eV $Å^{-1}$. For the Brillouin-zone sampling, 5×5×5 *k*-points for the unit cell and 2×2×2 *k*-points for the supercell were adopted to ensure convergence of the total energy.

Electrochemical tests

The positive electrode consisting of NVOPF/rGO (60 wt%), acetylene black (AB, 30 wt%), and polytetrafluoroethylene (PTFE, 10 wt%) was prepared by Roller Press. The electrochemical desodiated process of NVOPF/rGO cathode was performed in sodium-ion batteries (SIBs). The desodiated electrodes were washed three times with AN (Aldrich Co., anhydrous) and soaked in AN for 12 h in a glove box. Finally, the electrochemical performances for MIBs were tested by 2016 coin cells assembled with $NaV_2O_2(PO_4)_2F$/rGO as the cathode, glass fiber (GF)/A as the separator, 0.3 mol L^{-1} $Mg(TFSI)_2$ (Alfa Aesar Co.) in AN as the electrolyte and activated carbon (AC) cloth as both reference and counter electrode. AC cloth is usually selected as both the reference and counter electrodes, as the potential of AC cloth electrode (2.4 V *vs.* Mg^{2+}/Mg) is stable in AN-based electrolyte [13,38,39], and it can fast (de)adsorb $(TFSI)^-$ during (dis)charge process [39].

The negative electrode consists of NTP/C (70 wt%), AB (20 wt%), and PTFE (10 wt%). The open-circuit voltage of NTP/C//AC cell is about 0 *vs.* AC and the electrochemical performances of the negative electrode were tested within −1.4 to 0 V *vs.* AC in $Mg(TFSI)_2$/AN electrolyte. The $Mg_{0.79}NaTi_2(PO_4)_3$/C anode was obtained after magnesiation of NTP/C electrode.

The Mg-ion full cell consisting of $Mg_{0.79}NaTi_2(PO_4)_3$/C anode and $NaV_2O_2(PO_4)_2F$/rGO cathode was constructed. The working voltage was between 0.3 and 2.2 V in $Mg(TFSI)_2$/AN electrolyte. A multichannel battery testing system (LAND CT2001A) was used for galvanostatic discharge-charge tests. Cyclic voltammetry (CV) was performed with an Autolab PGSTAT 302N electrochemical workstation.

The preparation of Mg-hexamethyldisilazide (Mg-HMDS)-based electrolyte was carried out according to a previous report in an argon filled glove box [40]. Firstly, 1.24 g $(HMDS)_2Mg$ was dissolved in 4 mL of dimethoxyethane (DME). Next, 0.96 g anhydrous $AlCl_3$ was added to the pale yellow solution with continuous stirring for 36 h. Finally, 0.343 g $MgCl_2$ was added to the solution accompanied with continuous stirring for 48 h.

RESULTS AND DISCUSSION

Firstly, NVOPF/rGO microsphere precursors were prepared *via* a facile spray drying-annealing process and NVOPF was obtained by calcination without spray drying process (Figs S3 and S4). The Rietveld refinement result for NVOPF/rGO shows a tetragonal phase with the space group of *I*4/*mmm* (Fig. S5, Table S1) with Na1 and Na2 located at 8h and 8j sites, respectively [41,42]. The HAADF image and elemental maps (Fig. S6) indicate that the microspheres are encased in graphene. Raman spectrum indicates the I_D/I_G is 1.37, demonstrating the existence of rGO (Fig. S7) [43]. XPS spectrum (Fig. S8) reveals that the average valence state of V in NVOPF/rGO is +4 [44,45]. The $NaV_2O_2(PO_4)_2F$/rGO was obtained by electrochemical extration of 2 mol Na^+ from 1 mol NVOPF/rGO (charge to 4.5 V *vs.* Na^+/Na) (Fig. 1a). Fig. 1b displays the Rietveld refinement result of $NaV_2O_2(PO_4)_2F$/rGO. All diffraction peaks of the $NaV_2O_2(PO_4)_2F$/rGO are well indexed to tetragonal structure with the space group of *I4*/*mmm*. The corresponding structural parameters are shown in Table S2 and Fig. 1b, in which a=6.3029 Å, and c=10.7874 Å. The Rietveld refinement result meets the low reliability factors of goodness of fitting (GOF)=1.47, R_{wp}=11.21%, and R_p=8.52%, indicating the results of the Rietveld refinement are highly credible. The crystal structure of $NaV_2O_2(PO_4)_2F$/rGO is shown in Fig. 1c. In the *ab* plane, $[PO_4]$ tetrahedrons and $[VO_5F]$ octahedrons are connected by sharing one oxygen atom. Along the *c* direction, $[VO_5F]$ octahedrons are connected by sharing one fluorine atom. These connections form a stable frame and wide channels for Mg^{2+} diffusion. The remained 1 Na1 at 8h site could not be extracted when charging to 4.5 V in SIBs. The HAADF image and corresponding elemental maps (Fig. S9) show the size of ~1 μm $NaV_2O_2(PO_4)_2F$/rGO microsphere and the existence of Na, O, V, P, and F elements.

In order to evaluate Mg^{2+} diffusion kinetics in $NaV_2O_2(PO_4)_2F$/rGO, galvanostatic intermittent titration technique (GITT) was performed to investigate Mg^{2+} diffusion coefficients during the discharge process (Fig. 1d) [46,47]. The GITT curves and detailed calculations are shown in Fig. S10. During the discharge process, the diffusion coefficient of Mg^{2+} in $NaV_2O_2(PO_4)_2F$/rGO decreases from 7.95×10^{-10} to 1.13×10^{-11} $cm^2\ s^{-1}$ with the increasing concentration of Mg^{2+}. The average diffusion coefficient is calculated as 2.99×10^{-10} $cm^2\ s^{-1}$ (around 1×10^{-11} $cm^2\ s^{-1}$ for $MgCl^+$ in TiS_2 [11], 2.6×10^{-12} $cm^2\ s^{-1}$ for Mg^{2+} in Mo_6S_8 [48] and 4×10^{-11} $cm^2\ s^{-1}$ for $[Mg(DME)_x]^{2+}$ in MoS_2 [49]) over the whole discharge process. To analyze the diffusion behavior of Mg^{2+} in $NaV_2O_2(PO_4)_2F$/rGO, the Mg^{2+} migration pathway and corresponding energy barriers were optimized with NEB method in a 2×2×1 supercell [50]. Two possible diffusion pathways denoted as Path 1 (perpendicular to the *ab* plane) and Path 2 (parallel to the *ab* plane) were considered (Fig. 1e and Fig. S2) [36,37]. As shown in Fig. 1f, the diffusion energy barriers are 2.76 eV along the *c* direction (Path 1) and 0.78 eV along the *a* direction (Path 2), respectively. It indicates that $NaV_2O_2(PO_4)_2F$/rGO has a one-dimensional (1D) wide channel with fast Mg^{2+} diffusion at the *ab* plane. Meanwhile, minimum steric hindrance of transition metal polyanion based materials also facilitates the reduction of the Mg^{2+} diffusion energy barriers [51].

The Mg^{2+} storage performance of $NaV_2O_2(PO_4)_2F$/rGO was evaluated in $Mg(TFSI)_2$/AN. AC (2.4 V *vs.* Mg^{2+}/Mg) is selected as both the counter and reference electrodes. CV tests of stainless steel (SS) and Al foil as working electrodes within 0.4–4.4 V *vs.* Mg^{2+}/Mg (−2–2 V *vs.* AC) show that SS is a more stable current collector in $Mg(TFSI)_2$/AN (Fig. S11). Fig. 2a displays the CV curve of $NaV_2O_2(PO_4)_2F$/rGO electrode at 0.1 mV s^{-1}. Two pairs of distinct redox peaks at around 3.27/3.26 and 3.81/3.79 V are detected, corresponding to the redox of V^{4+}/V^{5+} [36,52]. Fig. 2b shows the galvanostatic charge-discharge (GCD) curves of NVOPF/rGO electrode at 0.1 A g^{-1}, where two distinct potential plateaus agree with the CV result. The GCD curves are further verified by using a three-electrode system cell (Fig. S12). $NaV_2O_2(PO_4)_2F$/rGO exhibits the discharge capacity of 83.4 mA h g^{-1}. It also has the average working potential of 3.3 V *vs.* Mg^{2+}/Mg which is higher than that of the reported cathode materials for MIBs (Table S3). Fig. 2c presents the rate capability of $NaV_2O_2(PO_4)_2F$/rGO at

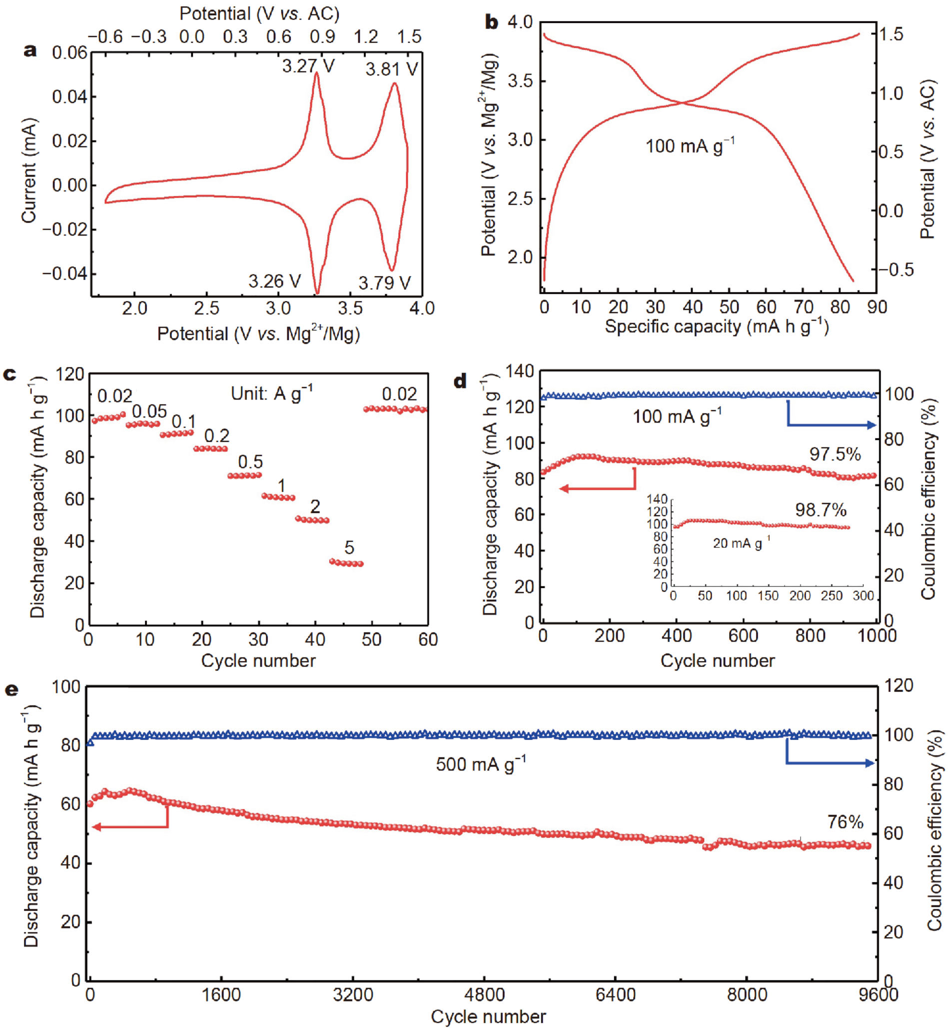

Figure 2 Magnesium-ion-storage performance of $NaV_2O_2(PO_4)_2F$/rGO. (a) CV curve of the $NaV_2O_2(PO_4)_2F$/rGO electrode between 1.8 and 3.9 V *vs.* Mg^{2+}/Mg at a scan rate of 0.1 mV s^{-1}. (b) GCD curves and (c) rate performances of the $NaV_2O_2(PO_4)_2F$/rGO electrode. Cycling performances at (d) 100 mA g^{-1} (the inset is the cycling performance at 20 mA g^{-1}) and (e) 500 mA g^{-1}.

different current densities varying from 0.02 to 5 A g^{-1}. The $NaV_2O_2(PO_4)_2F$/rGO shows the discharge capacities of 97.2, 95.4, 90.8, 83.9, 70.9, 61.5, 50.6, and 30.3 mA h g^{-1} at 0.02, 0.05, 0.1, 0.2, 0.5, 1, 2, and 5 A g^{-1}, respectively. The corresponding GCD curves are given in Fig. S13. The ultrahigh rate capability (30.3 mA h g^{-1} at 5 A g^{-1}, ~22 s per charge/discharge) is closely related to the wide Mg^{2+} diffusion channel and minimum steric hindrance of $NaV_2O_2(PO_4)_2F$/rGO (Table S3). $NaV_2O_2(PO_4)_2F$/rGO delivers a high capacity retention of 97.5% after 1000 cycles at 0.1 A g^{-1} (Fig. 2d) and the inset shows the capacity retention of 98.7% after 280 cycles at 0.02 A g^{-1}. To evaluate the cycling performance under a high current response, the cycling performance test was carried out at 0.5 A g^{-1} (Fig. 2e). The $NaV_2O_2(PO_4)_2F$/rGO exhibits ultralong cycling stability with a capacity retention of 76% for 9500 cycles. Such long cycle stability is superior to most of the cathode materials for MIBs (Table S3). GCD curves and cycling performances of $NaV_2O_2(PO_4)_2F$ electrode at 100 mA g^{-1} are shown in Fig. S14. Compared with $NaV_2O_2(PO_4)_2F$/rGO, $NaV_2O_2(PO_4)_2F$ shows a larger voltage hysteresis and a lower discharge capacity, which indicates that the addtion of rGO effectively improves the electronic conductivity and electrochemical performance of $NaV_2O_2(PO_4)_2F$.

To demonstrate the potential of $NaV_2O_2(PO_4)_2F$/rGO in practical applications, we designed the high-performance $Mg_{0.79}NaTi_2(PO_4)_3$/C anode for assembling an Mg-ion full cell (Fig. 3a). The XRD pattern and SEM image of NTP/C are shown in Figs S15 and S16, respectively. As

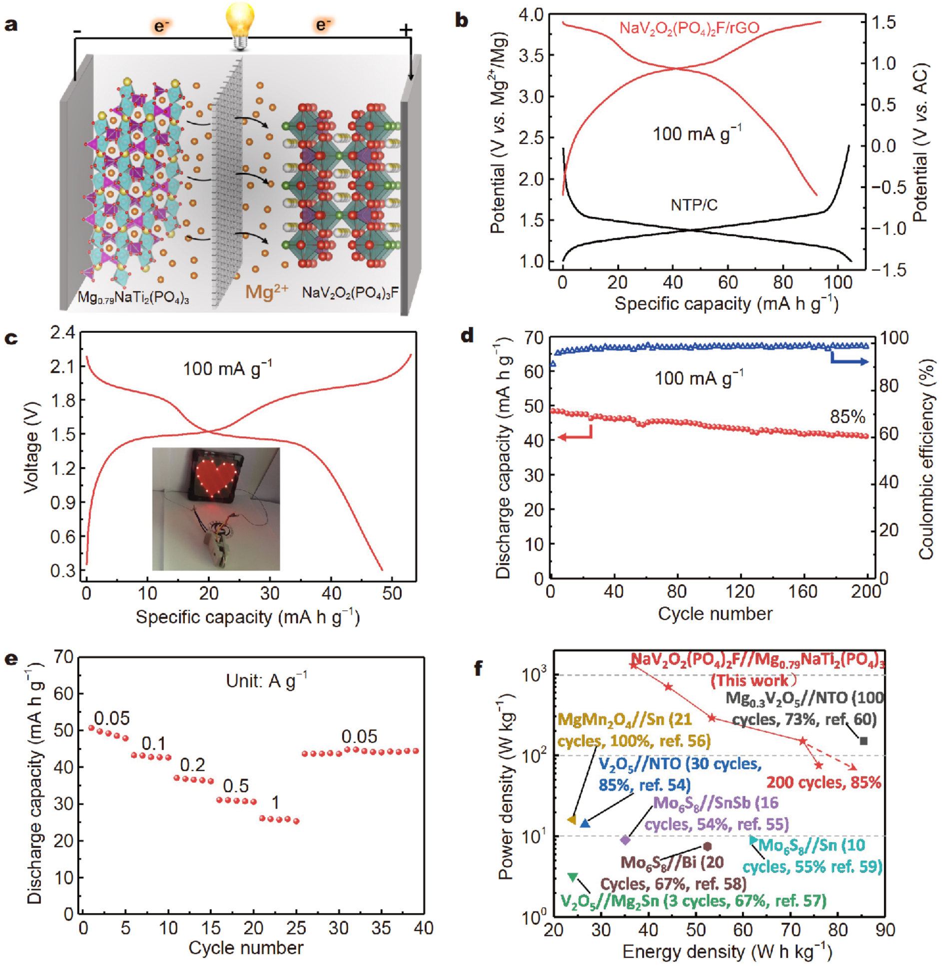

Figure 3 Electrochemical performances of the magnesium-ion full cell. (a) Schematic illustration of the Mg-ion full cell. (b) GCD curves of the $NaV_2O_2(PO_4)_2F$/rGO electrode and NTP/C electrode at 100 mA g^{-1}. (c) GCD curve of the Mg-ion full cell (the inset shows the 14 red LEDs illuminated by the two Mg-ion coin cells in series). (d) Cycling performances and (e) rate performance of the Mg-ion full cell (the capacity is based on the total mass of active material of the cathode and anode). (f) The Ragone plot for the Mg-ion full cell in the organic electrolyte system (Refs. [58,59] are counted based on the capacity of cathode).

shown in Fig. 3b, $Mg_{0.79}NaTi_2(PO_4)_3$ exhibits a charge capacity of 104 mA h g^{-1} and an average charge voltage of 1.4 V *vs.* Mg^{2+}/Mg and the discharge capacity of NVOPF/rGO is 92.4 mA h g^{-1} at 100 mA g^{-1}. The mass ratio of cathode and anode was 1:0.9, according to a matching of specific capacity. $Mg_{0.79}NaTi_2(PO_4)_3$ was determined by calculation based on the discharge capacity of NTP/C. During the discharge process of full cell, Mg^{2+} ions were removed from $Mg_{0.79}NaTi_2(PO_4)_3$/C and inserted into $NaV_2O_2(PO_4)_2F$/rGO. An inverse process occurs during the charge process. The redox reactions can be described as follows:

$$\text{Cathode}: NaV_2O_2(PO_4)_2F + 0.63Mg^{2+} + 1.26e^- \rightarrow Mg_{0.63}NaV_2O_2(PO_4)_2F, \tag{1}$$

$$\text{Anode}: 0.8Mg_{0.79}NaTi_2(PO_4)_3 \rightarrow 0.8NaTi_2(PO_4)_3 + 0.63Mg^{2+} + 1.26e^-, \tag{2}$$

$$\text{Overall}: NaV_2O_2(PO_4)_2F + 0.8Mg_{0.79}NaTi_2(PO_4)_3 \rightarrow Mg_{0.63}NaV_2O_2(PO_4)_2F + 0.8NaTi_2(PO_4)_3. \tag{3}$$

Fig. S17 displays the CV curve of the NTP/C electrode. Fig. S18 shows the cyclic performance of the NTP/C electrode at 0.1 A g^{-1}. The capacity retention of 91% after 100 cycles can be obtained. The NTP/C electrode delivers an initial discharge capacity of 83.6 mA h g^{-1} at 500 mA g^{-1} (Fig. S19). Capacity decay may be caused by structural deterioration or volume changes during the charge and discharge and a similar phenomenon has been studied in SIBs [53]. GITT test demonstrates that NTP/C has fast Mg^{2+} diffusion kinetics (average 1.40×10^{-9} cm^2 s^{-1}) (Fig. S20). In addition, the Mg^{2+} storage mechanism of NTP/C was studied by *in situ* XRD for the first time. The results (Fig. S21) show that the reaction mechanism is a two-phase reaction. The HAADF image of the discharged NTP/C and corresponding elemental maps (Fig. S22) show the existence of Mg, Na, Ti, O and P elements. Some reported work [30,53] about NTP in SIBs indicates that Na will not be extracted from NTP/C during the charge and discharge process. Fig. 3c shows the GCD curve of Mg-ion full cell at 100 mA g^{-1}. The Mg-ion full cell exhibits a discharge capacity of 48.5 mA h g^{-1} with an average discharge voltage of 1.5 V. 14 red-light-emitting diodes (LEDs) were illuminated by two Mg-ion coin cells in series (inset of Fig. 3c). After 200 cycles, the capacity retention rate is 85% at 0.1 A g^{-1} (Fig. 3d). Rate performance of Mg-ion full cell is shown in Fig. 3e. At 1 A g^{-1}, the discharge capacity can remain 26.3 mA h g^{-1}. Fig. 3f displays the comparison of our Mg-ion full cell with previously reported Mg-ion full cells [54–60]. For $NaV_2O_2(PO_4)_2F//Mg_{0.79}NaTi_2(PO_4)_3$ full cell, a high energy density of 76 W h kg^{-1} can be obtained at 50 mA g^{-1} based on the total active material mass of cathode and anode. $NaV_2O_2(PO_4)_2F//Mg_{0.79}NaTi_2(PO_4)_3$ full cell has the highest power density (1300 W kg^{-1}) in organic electrolyte system and good capacity retention (85% for 200 cycles). The excellent performances of Mg-ion full cell indicate a potential application prospect.

Finally, we chose Mg-HMDS-based electrolyte to verify the feasibility of the MIBs with Mg metal as anode and $NaV_2O_2(PO_4)_2F$/rGO as cathode. As the electrochemical stability window of Mg-HMDS-based electrolyte is 3.5 V *vs.* Mg^{2+}/Mg, a cutoff voltage of 3.5 V *vs.* Mg^{2+}/Mg is set. The discharge curves of $NaV_2O_2(PO_4)_2F$/rGO with the discharge capacity of 65.2 mA h g^{-1} and the cyclic performance of $NaV_2O_2(PO_4)_2F$/rGO at 20 mA g^{-1} are given in Fig. S23. The capacity in Mg-HMDS-based electrolyte is lower than that in $Mg(TFSI)_2$/AN electrolyte due to the electrochemical window limitation of Mg-HMDS-based electrolyte. The results demonstrate that $NaV_2O_2(PO_4)_2F$/rGO is a potential cathode material for high-energy-density MIBs. In order to realize the applications of $NaV_2O_2(PO_4)_2F$/rGO in practice, it is critical to develop a high-voltage electrolyte with good compatibility. Recently, some researchers have developed highly stable Mg electrolytes, such as $Mg(CB_{11}H_{11}F)_2$ [61], $Mg[B(HFIP)_4]_2$ [62] and $Mg[B(O_2C_2(CF_3)_4)_2]_2$ [63]. Unfortunately, their compatibility with the high-voltage cathode material is very poor. In order to achieve Mg electrolyte with high stability and good compatibility, the structures of anion and solvent should be modified. That is also what we are trying to achieve in the next work.

To provide guidance for designing cathode materials for MIBs with superior electrochemical performance, the Mg^{2+} storage mechanism of $NaV_2O_2(PO_4)_2F$/rGO was studied by *in situ* XRD, *ex situ* XANES and XPS technologies. As shown in Fig. 4a, the (200), (202), (220) and (301) diffraction peaks gradually shift to a high angle and (105) diffraction peak splits into two peaks during the charge process. After discharge, all diffraction peaks return to their original positions, indicating the full reversible phase change process. Meanwhile, the experiment shows no appearance of new phase during the charge/discharge processes. These results indicate that the Mg^{2+} storage mechanism of $NaV_2O_2(PO_4)_2F$/rGO is a single-phase (de)insertion reaction. The variations of lattice parameters and volume in the charge/discharge processes calculated by *in situ* XRD data are shown in Fig. 4b. The lattice parameters *a* and *b* continuously increase along with the discharge process and the increase ratios of *a* and *b* are 1.83% and 1.76%. The lattice parameter *c* decreases with a decrease ratio of 1.77%. These results indicate that Mg^{2+} ions tend to migrate in the *ab* plane, leading to the expansion of *ab* planes and shrinkage of *c* planes owing to a strong coulomb interaction between Mg^{2+} and V–O bonds. It is also consistent with the DFT calculation results [39,40]. Compared with the charged state, the unit cell volume of $NaV_2O_2(PO_4)_2F$/rGO increases by 1.79% (2.79% [37] and 2.40% [36] in SIBs) at the end of discharged process. The small volume variation leads to a stable Mg^{2+} migration and storage, thus excellent cycle performance is obtained. The SEM images of $NaV_2O_2(PO_4)_2F$/rGO after 280 cycles indicate that $NaV_2O_2(PO_4)_2F$/rGO still maintains the unbroken morphology (Fig. S24), further demonstrating the stable framework structure of $NaV_2O_2(PO_4)_2F$/rGO, indicating a very little mechanical stress produced in $NaV_2O_2(PO_4)_2F$/rGO during the cycle.

Ex situ XRD patterns corresponding to (de)magnesiation process are shown in Fig. S25. The changes of each diffraction peak are consistent with the *in situ* XRD results. To deeply investigate the crystal structure of $NaV_2O_2(PO_4)_2F$/rGO at full discharged state (1.8 V), the Rietveld refinement was carried out and the corresponding crystal structure is shown in Fig. S26. The results reveal that full discharged $NaV_2O_2(PO_4)_2F$/rGO still maintains a tetragonal phase with the space group of *I*4/*mmm* and Mg^{2+} ions are randomly distributed at 8h and 8j sites with relative occupancy of 14.4% for 8h and 17%

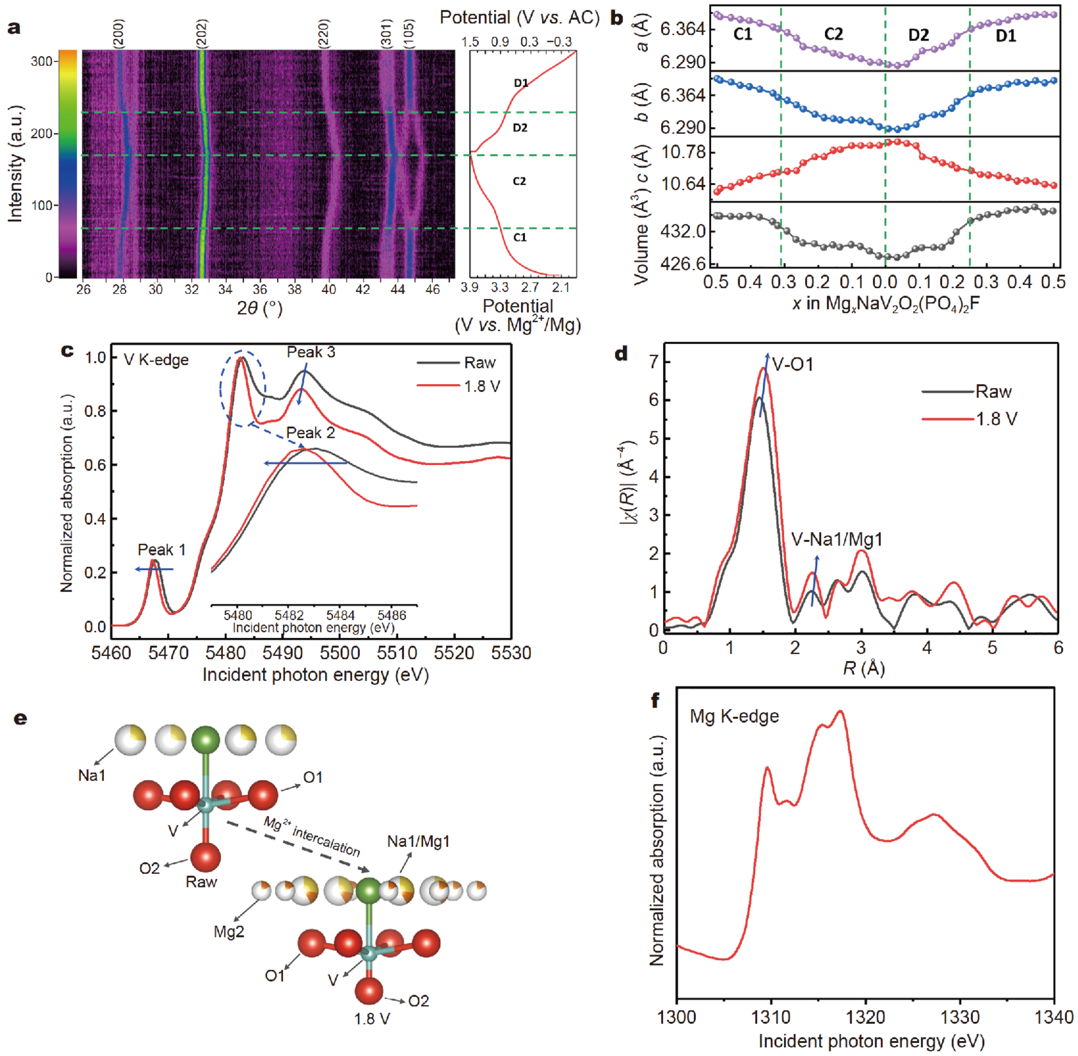

Figure 4 Magnesium-ion-storage mechanism of $NaV_2O_2(PO_4)_2F$/rGO. (a) *In situ* XRD patterns and the corresponding GCD curve. (b) Cell parameters and cell volume during the charge and discharge process. (c) Vanadium K-edge XANES spectra of the raw $NaV_2O_2(PO_4)_2F$/rGO (black line) and fully discharged $NaV_2O_2(PO_4)_2F$/rGO (red line). (d) The corresponding FT-EXAFS spectra in R space. (e) Description of the coordination environment change of V sites. (f) Mg K-edge XANES spectrum for fully discharged $NaV_2O_2(PO_4)_2F$/rGO.

for 8j (Figs S26 and S27, Table S4). It further indicates that the Mg^{2+} storage mechanism of $NaV_2O_2(PO_4)_2F$/rGO is a single-phase insertion-extraction reaction.

To understand the structure changes of $NaV_2O_2(PO_4)_2F$/rGO after magnesiation in depth, the vanadium K-edge XANES tests were performed to reveal the valance and bond structure changes of pristine and magnesiated $NaV_2O_2(PO_4)_2F$/rGO (Fig. 4c). The K-edge of the vanadium of magnesiated $NaV_2O_2(PO_4)_2F$/rGO slightly shifts to low energy compared with that of pristine one, indicating a decrease in the average valence of V after magnesiation. The changes of pre-edge (peak 1) and the edge resonance (peak 2) indicate some changes of coordination environment and valence state [64]. The intensity of the peak 1 is inversely correlated with the symmetry of the octahedron of the vanadium site [65,66]. After magnesiation, there is no significant change in the intensity of peak 1, indicating that the octahedron of the vanadium site maintains good symmetry and the framework of $NaV_2O_2(PO_4)_2F$/rGO is stable. The edge resonance, caused by the energy absorption by core electrons [67], presents major variation in shape. Some similar changes in peak shape caused by the decrease in vanadium valence were reported in other literatures [35,65,67,68]. The first EXAFS oscillation [69,70] (peak 3) of $NaV_2O_2(PO_4)_2F$/rGO at 1.8 V moves to lower energy compared with raw $NaV_2O_2(PO_4)_2F$/rGO, which is similar to some other reports [60,69].

As shown in Fig. 4d, Fourier transform EXAFS (FT-EXAFS) spectra were employed to discuss the changes of the coordination environment of vanadium in pristine and magnesiated $NaV_2O_2(PO_4)_2F$/rGO. The schematic of coordination environment of vanadium is shown in Fig. 4e. The length of V–O1 bond (at around 1.5 Å) slightly increases after magnesiation, indicating the increase of the unit cell parameters *a* and *b*. This result is consistent with the ones obtained by *in situ* XRD in Fig. 4b. Meanwhile, the distance of V–Na1/Mg1 (at around 2.2 Å) increases compared with V–Na1 at raw after magnesiation. The variation is caused by stronger interaction between Mg^{2+} and O/F. As shown in Fig. 4d, there is no significant change in the distance of the shell layers around the vanadium site after magnesiation, verifying the small volume change in $NaV_2O_2(PO_4)_2F$/rGO during Mg^{2+} insertion process. Moreover, the *ex-situ* XPS spectra of Mg 1s and V 2p reveal the average valence state of vanadium decreases and the insertion behavior of Mg^{2+} occurs during the discharge process (Fig. S28). When charged to 3.9 V, the peak of Mg 1s becomes significantly weaker and the peak of V 2p shifts towards high binding energy, which shows the deinsertion of Mg^{2+} ions and the average valence of vanadium increases. The HAADF image of the magnesiated $NaV_2O_2(PO_4)_2F$/rGO microsphere and the corresponding elemental maps (Fig. S29) show the existence of Mg, Na, V, O, P and F elements. EDX spectrum (Fig. S30) shows the atomic ratio of Mg to Na is 0.68, which is consistent with the calculated 0.63 according to the discharge capacity. Moreover, Mg K-edge XANES spectrum for fully discharged $NaV_2O_2(PO_4)_2F$/rGO (Fig. 4f) reveals resonance characteristic of Mg^{2+} to be consistent with previous Mg K-edge studies [6], and the inductively coupled plasma (ICP) results (Table S5) demonstrate that no Na^+ ions are inserted in $NaV_2O_2(PO_4)_2F$/rGO during discharge and the molar ratio of Mg to Na is 0.57, thus offering one more proof that Mg^{2+} ions are inserted into $NaV_2O_2(PO_4)_2F$/rGO.

With the above results, a schematic illustration summarizes the topotactic insertion reaction mechanism (Fig. 5). From state 1 to state 2, 1 mol Na1 (8h site) and 1 mol Na2 (8j site) are extracted from 1 mol NVOPF/rGO by an electrochemical method and the remaining 1 mol Na1 cannot be extracted when charging to 4.5 V in SIBs. In state 2, the Mg^{2+} host of a tetragonal $NaV_2O_2(PO_4)_2F$/rGO with 8h and 8j vacant sites is obtained. After magnesiation, Mg^{2+} ions are randomly distributed at 8h and 8j sites with relative occupancy of 14.4% for 8h and 17% for 8j (state 3). The Mg^{2+} storage mechanism of $NaV_2O_2(PO_4)_2F$/rGO is a single-phase insertion-extraction reaction. Topotactic insertion reaction can maintain the crystal structure of $NaV_2O_2(PO_4)_2F$/rGO during (dis) charge, guaranteeing excellent long-term cycling performance. 1D continuous diffusion channels, low Mg^{2+} diffusion energy barriers and minimum steric hindrance of $NaV_2O_2(PO_4)_2F$/rGO result in ultrahigh rate performance. In addition, due to the inductive effect of polyanions, increasing the electronegativity of polyanions is an effective way to raise the redox potentials [68,71]. The introduction of F^- anion can effectively increase the electronegativity of $(PO_4)^{3-}$, which is the origin of high working voltage for $NaV_2O_2(PO_4)_2F$/rGO.

CONCLUSIONS

In summary, $NaV_2O_2(PO_4)_2F$/rGO, proposed as a cathode material for MIBs for the first time, shows fast kinetics of Mg^{2+} intercalation, the highest working voltage and ultralong cyclic stability. The excellent electrochemical performance makes $NaV_2O_2(PO_4)_2F$/rGO a promising cathode material for MIBs. In addition, the assembled Mg-ion full cell exhibits an energy density of 76 W h kg^{-1}

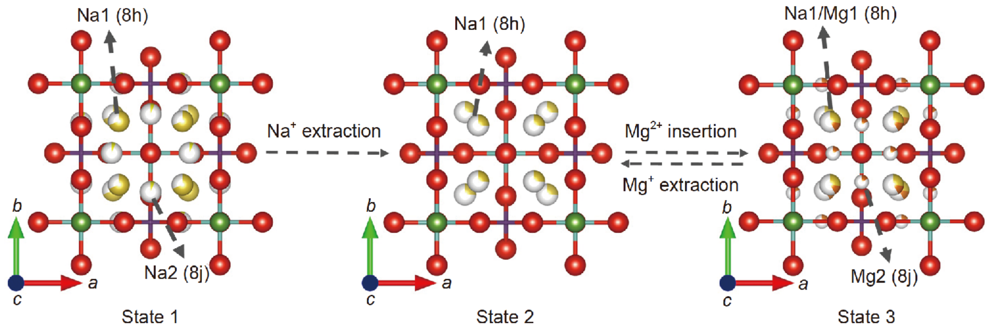

Figure 5 A schematic of distribution of Na and Mg in different states. State 1: $Na_3V_2O_2(PO_4)_2F$/rGO, state 2: $NaV_2O_2(PO_4)_2F$/rGO, state 3: magnesiated $NaV_2O_2(PO_4)_2F$/rGO.

and the highest power density (1300 W kg^{-1}) in the organic electrolyte system, and the performance of the Mg-ion full cell has room for further improvement by selecting a lower redox potential and higher capacity anode. 1D continuous diffusion channels and minimum steric hindrance of fluorophosphate can effectively reduce the diffusion energy barriers of Mg^{2+}. And the existence of F^{-} can increase the electronegativity of $(PO_4)^{3-}$, which can raise the working voltage. These conclusions can provide reference for the design and preparation of new high-voltage cathode materials for MIBs. Furthermore, the fluorophosphate system is pointed out to overcome the challenge of sluggish kinetics and low working voltage in multivalent ions (Zn^{2+}, Ca^{2+}, Al^{3+}, etc.) batteries.

Received 9 February 2020; accepted 21 March 2020;

1 Yoo HD, Shterenberg I, Gofer Y, *et al.* Mg rechargeable batteries: An on-going challenge. Energy Environ Sci, 2013, 6: 2265–2279

2 Muldoon J, Bucur CB, Oliver AG, *et al.* Electrolyte roadblocks to a magnesium rechargeable battery. Energy Environ Sci, 2012, 5: 5941–5950

3 Ling C, Banerjee D, Matsui M. Study of the electrochemical deposition of Mg in the atomic level: Why it prefers the non-dendritic morphology. Electrochim Acta, 2012, 76: 270–274

4 Wang Y, Chen R, Chen T, *et al.* Emerging non-lithium ion batteries. Energy Storage Mater, 2016, 4: 103–129

5 Aurbach D, Lu Z, Schechter A, *et al.* Prototype systems for rechargeable magnesium batteries. Nature, 2000, 407: 724–727

6 Andrews JL, Mukherjee A, Yoo HD, *et al.* Reversible Mg-ion insertion in a metastable one-dimensional polymorph of V_2O_5. Chem, 2018, 4: 564–585

7 Kim JS, Chang WS, Kim RH, *et al.* High-capacity nanostructured manganese dioxide cathode for rechargeable magnesium ion batteries. J Power Sources, 2015, 273: 210–215

8 Liang Y, Feng R, Yang S, *et al.* Rechargeable Mg batteries with graphene-like MoS_2 cathode and ultrasmall Mg nanoparticle anode. Adv Mater, 2011, 23: 640–643

9 Xue X, Chen R, Yan C, *et al.* One-step synthesis of 2-ethylhexylamine pillared vanadium disulfide nanoflowers with ultralarge interlayer spacing for high-performance magnesium storage. Adv Energy Mater, 2019, 9: 1900145

10 Tang H, Xu N, Pei C, *et al.* $H_2V_3O_8$ nanowires as high-capacity cathode materials for magnesium-based battery. ACS Appl Mater Interfaces, 2017, 9: 28667–28673

11 Yoo HD, Liang Y, Dong H, *et al.* Fast kinetics of magnesium monochloride cations in interlayer-expanded titanium disulfide for magnesium rechargeable batteries. Nat Commun, 2017, 8: 339

12 Zhou L, Liu Q, Zhang Z, *et al.* Interlayer-spacing-regulated $VOPO_4$ nanosheets with fast kinetics for high-capacity and durable rechargeable magnesium batteries. Adv Mater, 2018, 30: 1801984

13 Zeng J, Yang Y, Lai S, *et al.* A promising high-voltage cathode material based on mesoporous $Na_3V_2(PO_4)_3$/C for rechargeable magnesium batteries. Chem Eur J, 2017, 23: 16898–16905

14 Huang ZD, Masese T, Orikasa Y, *et al.* Vanadium phosphate as a promising high-voltage magnesium ion (de)-intercalation cathode host. RSC Adv, 2015, 5: 8598–8603

15 Wang Y, Xue X, Liu P, *et al.* Atomic substitution enabled synthesis of vacancy-rich two-dimensional black TiO_{2-x} nanoflakes for high-performance rechargeable magnesium batteries. ACS Nano, 2018, 12: 12492–12502

16 Li Y, Nuli YN, Yang J, *et al.* $MgFeSiO_4$ prepared *via* a molten salt method as a new cathode material for rechargeable magnesium batteries. Chin Sci Bull, 2011, 56: 386–390

17 Mizuno Y, Okubo M, Hosono E, *et al.* Electrochemical Mg^{2+} intercalation into a bimetallic CuFe Prussian blue analog in aqueous electrolytes. J Mater Chem A, 2013, 1: 13055

18 Okamoto S, Ichitsubo T, Kawaguchi T, *et al.* Intercalation and push-out process with spinel-to-rocksalt transition on Mg insertion into spinel oxides in magnesium batteries. Adv Sci, 2015, 2: 1500072

19 Orikasa Y, Masese T, Koyama Y, *et al.* High energy density rechargeable magnesium battery using earth-abundant and non-toxic elements. Sci Rep, 2015, 4: 5622

20 Wang Y, Liu Z, Wang C, *et al.* Highly branched VS_4 nanodendrites with 1D atomic-chain structure as a promising cathode material for long-cycling magnesium batteries. Adv Mater, 2018, 30: 1802563

21 An Q, Li Y, Deog Yoo H, *et al.* Graphene decorated vanadium oxide nanowire aerogel for long-cycle-life magnesium battery cathodes. Nano Energy, 2015, 18: 265–272

22 Esparcia Jr. EA, Chae MS, Ocon JD, *et al.* Ammonium vanadium bronze ($NH_4V_4O_{10}$) as a high-capacity cathode material for non-aqueous magnesium-ion batteries. Chem Mater, 2018, 30: 3690–3696

23 Kaveevivitchai W, Jacobson AJ. High capacity rechargeable magnesium-ion batteries based on a microporous molybdenum-vanadium oxide cathode. Chem Mater, 2016, 28: 4593–4601

24 Rasul S, Suzuki S, Yamaguchi S, *et al.* Manganese oxide octahedral molecular sieves as insertion electrodes for rechargeable Mg batteries. Electrochim Acta, 2013, 110: 247–252

25 Sun X, Bonnick P, Nazar LF. Layered TiS_2 positive electrode for Mg batteries. ACS Energy Lett, 2016, 1: 297–301

26 Kim C, Phillips PJ, Key B, *et al.* Direct observation of reversible magnesium ion intercalation into a spinel oxide host. Adv Mater, 2015, 27: 3377–3384

27 Truong QD, Devaraju MK, Honma I. Nanocrystalline $MgMnSiO_4$ and $MgCoSiO_4$ particles for rechargeable Mg-ion batteries. J Power Sources, 2017, 361: 195–202

28 Wang RY, Wessells CD, Huggins RA, *et al.* Highly reversible open framework nanoscale electrodes for divalent ion batteries. Nano Lett, 2013, 13: 5748–5752

29 Yin Y, Xiong F, Pei C, *et al.* Robust three-dimensional graphene skeleton encapsulated $Na_3V_2O_2(PO_4)_2F$ nanoparticles as a high-rate and long-life cathode of sodium-ion batteries. Nano Energy, 2017, 41: 452–459

30 Xu C, Xu Y, Tang C, *et al.* Carbon-coated hierarchical $NaTi_2(PO_4)_3$ mesoporous microflowers with superior sodium storage performance. Nano Energy, 2016, 28: 224–231

31 Kresse G, Joubert D. From ultrasoft pseudopotentials to the projector augmented-wave method. Phys Rev B, 1999, 59: 1758–1775

32 Kresse G, Furthmüller J. Efficient iterative schemes for *ab initio* total-energy calculations using a plane-wave basis set. Phys Rev B, 1996, 54: 11169–11186

33 Kresse G, Furthmüller J. Efficiency of *ab-initio* total energy calculations for metals and semiconductors using a plane-wave basis

set. Comput Mater Sci, 1996, 6: 15–50

34 Perdew JP, Burke K, Ernzerhof M. Generalized gradient approximation made simple. Phys Rev Lett, 1996, 77: 3865–3868

35 Sharma N, Serras P, Palomares V, *et al.* Sodium distribution and reaction mechanisms of a $Na_3V_2O_2(PO_4)_2F$ electrode during use in a sodium-ion battery. Chem Mater, 2014, 26: 3391–3402

36 Chao D, Lai CHM, Liang P, *et al.* Sodium vanadium fluorophosphates (NVOPF) array cathode designed for high-rate full sodium ion storage device. Adv Energy Mater, 2018, 8: 1800058

37 Hou Y, Chang K, Wang Z, *et al.* Rapid microwave-assisted refluxing synthesis of hierarchical mulberry-shaped $Na_3V_2(PO_4)_2O_2F$@C as high performance cathode for sodium & lithium-ion batteries. Sci China Mater, 2019, 62: 474–486

38 Ruch PW, Cericola D, Hahn M, *et al.* On the use of activated carbon as a quasi-reference electrode in non-aqueous electrolyte solutions. J Electroanal Chem, 2009, 636: 128–131

39 Gershinsky G, Yoo HD, Gofer Y, *et al.* Electrochemical and spectroscopic analysis of Mg^{2+} intercalation into thin film electrodes of layered oxides: V_2O_5 and MoO_3. Langmuir, 2013, 29: 10964–10972

40 Zhao-Karger Z, Zhao X, Wang D, *et al.* Performance improvement of magnesium sulfur batteries with modified non-nucleophilic electrolytes. Adv Energy Mater, 2015, 5: 1401155

41 Massa W, Yakubovich OV, Dimitrova OV. Crystal structure of a new sodium vanadyl(IV) fluoride phosphate $Na_3\{V_2O_2F[PO_4]_2\}$. Solid State Sci, 2002, 4: 495–501

42 Sauvage F, Quarez E, Tarascon JM, *et al.* Crystal structure and electrochemical properties *vs.* Na^+ of the sodium fluorophosphate $Na_{1.5}VOPO_4F_{0.5}$. Solid State Sci, 2006, 8: 1215–1221

43 Tan S, Jiang Y, Wei Q, *et al.* Multidimensional synergistic nanoarchitecture exhibiting highly stable and ultrafast sodium-ion storage. Adv Mater, 2018, 30: 1707122

44 Jin H, Dong J, Uchaker E, *et al.* Three dimensional architecture of carbon wrapped multilayer $Na_3V_2O_2(PO_4)_2F$ nanocubes embedded in graphene for improved sodium ion batteries. J Mater Chem A, 2015, 3: 17563–17568

45 Tong Z, Qi Y, Zhao J, *et al.* One-step synthesis of carbon-coated $Na_3(VOPO_4)_2F$ using biomass as a reducing agent and their electrochemical properties. Waste Biomass Valor, 2020, 11: 2201–2209

46 Deiss E. Spurious chemical diffusion coefficients of Li^+ in electrode materials evaluated with GITT. Electrochim Acta, 2005, 50: 2927–2932

47 Weppner W. Determination of the kinetic parameters of mixed-conducting electrodes and application to the system Li_3Sb. J Electrochem Soc, 1977, 124: 1569

48 Levi MD, Lancry E, Gizbar H, *et al.* Phase transitions and diffusion kinetics during Mg^{2+}- and Li^+-ion insertions into the Mo_6S_8 Chevrel phase compound studied by PITT. Electrochim Acta, 2004, 49: 3201–3209

49 Fichtner A, Härdtle W, Bruelheide H, *et al.* Neighbourhood interactions drive overyielding in mixed-species tree communities. Nat Commun, 2018, 9: 5115

50 Henkelman G, Uberuaga BP, Jónsson H. A climbing image nudged elastic band method for finding saddle points and minimum energy paths. J Chem Phys, 2000, 113: 9901–9904

51 Wang F, Hu E, Sun W, *et al.* A rechargeable aqueous Zn^{2+}-battery with high power density and a long cycle-life. Energy Environ Sci, 2018, 11: 3168–3175

52 Qi Y, Tong Z, Zhao J, *et al.* Scalable room-temperature synthesis of multi-shelled $Na_3(VOPO_4)_2F$ microsphere cathodes. Joule, 2018, 2: 2348–2363

53 Senguttuvan P, Rousse G, Arroyo y de Dompablo ME, *et al.* Low-potential sodium insertion in a NASICON-type structure through the Ti(III)/Ti(II) redox couple. J Am Chem Soc, 2013, 135: 3897–3903

54 Chen C, Wang J, Zhao Q, *et al.* Layered $Na_2Ti_3O_7$/$MgNaTi_3O_7$/$Mg_{0.5}NaTi_3O_7$ nanoribbons as high-performance anode of rechargeable Mg-ion batteries. ACS Energy Lett, 2016, 1: 1165–1172

55 Cheng Y, Shao Y, Parent LR, *et al.* Interface promoted reversible Mg insertion in nanostructured tin-antimony alloys. Adv Mater, 2015, 27: 6598–6605

56 Nacimiento F, Cabello M, Pérez-Vicente C, *et al.* On the mechanism of magnesium storage in micro- and nano-particulate tin battery electrodes. Nanomaterials, 2018, 8: 501

57 Nguyen DT, Song SW. Magnesium stannide as a high-capacity anode for magnesium-ion batteries. J Power Sources, 2017, 368: 11–17

58 Shao Y, Gu M, Li X, *et al.* Highly reversible Mg insertion in nanostructured Bi for Mg ion batteries. Nano Lett, 2014, 14: 255–260

59 Singh N, Arthur TS, Ling C, *et al.* A high energy-density tin anode for rechargeable magnesium-ion batteries. Chem Commun, 2013, 49: 149–151

60 Xu Y, Deng X, Li Q, *et al.* Vanadium oxide pillared by interlayer Mg^{2+} ions and water as ultralong-life cathodes for magnesium-ion batteries. Chem, 2019, 5: 1194–1209

61 Luo J, Bi Y, Zhang L, *et al.* A stable, non-corrosive perfluorinated pinacolatoborate Mg electrolyte for rechargeable Mg batteries. Angew Chem Int Ed, 2019, 58: 6967–6971

62 Zhao-Karger Z, Gil Bardaji ME, Fuhr O, *et al.* A new class of non-corrosive, highly efficient electrolytes for rechargeable magnesium batteries. J Mater Chem A, 2017, 5: 10815–10820

63 Hahn NT, Seguin TJ, Lau KC, *et al.* Enhanced stability of the Carba-*closo*-dodecaborate anion for high-voltage battery electrolytes through rational design. J Am Chem Soc, 2018, 140: 11076–11084

64 Zhang G, Xiong T, Yan M, *et al.* α-MoO_{3-x} by plasma etching with improved capacity and stabilized structure for lithium storage. Nano Energy, 2018, 49: 555–563

65 Liu Q, Li ZF, Liu Y, *et al.* Graphene-modified nanostructured vanadium pentoxide hybrids with extraordinary electrochemical performance for Li-ion batteries. Nat Commun, 2015, 6: 6127

66 Passerini S. XAS and electrochemical characterization of lithium intercalated V_2O_5 xerogels. Solid State Ion, 1996, 90: 5–14

67 Wong J, Lytle FW, Messmer RP, *et al.* K-edge absorption spectra of selected vanadium compounds. Phys Rev B, 1984, 30: 5596–5610

68 Park YU, Seo DH, Kwon HS, *et al.* A new high-energy cathode for a Na-ion battery with ultrahigh stability. J Am Chem Soc, 2013, 135: 13870–13878

69 Giorgetti M. *In situ* X-ray absorption spectroscopy characterization of V_2O_5 xerogel cathodes upon lithium intercalation. J Electrochem Soc, 1999, 146: 2387–2392

70 Stallworth PE, Kostov S, denBoer ML, *et al.* X-ray absorption and magnetic resonance spectroscopic studies of $Li_xV_6O_{13}$. J Appl Phys, 1998, 83: 1247–1255

71 Melot BC, Tarascon JM. Design and preparation of materials for advanced electrochemical storage. Acc Chem Res, 2013, 46: 1226–1238

Acknowledgements This work was supported by the National Key Research and Development Program of China (2016YFA0202603 and

2016YFA0202601), the National Natural Science Fund for Distinguished Young Scholars (51425204), the National Natural Science Foundation of China (51832004, 51602239 and 51672307), and the International Science & Technology Cooperation Program of China (2013DFA50840).

Author contributions Mai L, An Q and Wang J conceived the study. Tan S and Wang J performed the electrochemical measurements together with Huang D and Zhang G conducted the Rietveld refinement. Jiang Y performed the first-principles calculations. Yin Y designed the synthesis method. Zhang G and Li Q performed the V K-edge experiments. Zhang Q and Gu L conducted the TEM measurements and analysis. Wang J, Tan S, An Q and Xiong F participated in the all data analysis and wrote the manuscript together with Mai L. Mai L and An Q provided insights for the experiments and supervised the research. All authors agreed with the final version of the manuscript.

Conflict of interest The authors declare that they have no conflict of interest.

Supplementary information Experimental details are available in the online version of the paper.

Junjun Wang received his BS degree in materials science and engineering from Henan Polytechnic University in 2017. He is currently working toward the master's degree in materials science and engineering at Wuhan University of Technology (WUT). His current research focuses on rechargeable magnesium and calcium batteries.

Shuangshuang Tan received his BS degree in materials science and engineering from WUT in 2016. He is currently working toward the PhD degree at WUT and his current research focuses on rechargeable magnesium batteries and metal-sulfur batteries.

Qinyou An is an associate professor of materials science and engineering at WUT. He received his PhD degree from WUT in 2014. He carried out his postdoctoral research in the laboratory of Prof. Yan Yao at the University of Houston in 2014–2015. Currently, his research interest includes energy-storage materials and devices.

Liqiang Mai is Changjiang Scholar Chair Professor of materials science and engineering at WUT. He is the winner of the National Natural Science Fund for Distinguished Young Scholars and Fellow of the Royal Society of Chemistry. He received his PhD from WUT in 2004 and carried out his postdoctoral research with Prof. Zhong Lin Wang at Georgia Institute of Technology in 2006–2007. He worked as an advanced research scholar with Prof. Charles M. Lieber at Harvard University in 2008–2011 and Prof. Peidong Yang at University of California, Berkeley in 2017. His current research interests focus on new nanomaterials for electrochemical energy storage and micro/nano energy devices.

高电压镁离子电池正极材料$NaV_2O_2(PO_4)_2F$/rGO快速和稳定的Mg^{2+}嵌入

王军军[1†], 谭双双[1†], 张国彬[1], 姜亚龙[1], 殷亚朦[1], 熊方宇[1], 李启东[1], 黄丹[1], 张庆华[2], 谷林[2], 安琴友[1*], 麦立强[1*]

摘要 缓慢的Mg^{2+}扩散动力学和低的工作电势严重阻碍高能量密度镁离子电池(MIBs)的发展. 因此, 开发具有快速Mg^{2+}扩散和高工作电势的正极材料是克服MIBs发展阻碍的关键. 在本文中, 首次提出四方相的$NaV_2O_2(PO_4)_2F$/rGO作为一个有效的Mg^{2+}宿主. 它展现出3.3 V *vs.* Mg^{2+}/Mg的最高平均放电电压, 2.99×10^{-10} cm^2 s^{-1}的平均Mg^{2+}扩散系数和9500个循环的超长循环寿命. 原位X射线衍射(XRD)表明$NaV_2O_2(PO_4)_2F$/rGO的储镁机制为单相的嵌入/脱出反应. 密度泛函理论(DFT)计算表明Mg^{2+}倾向于沿*a*方向迁移. X射线吸收近边结构(XANES)表明镁化后钒的平均价态降低且钒位点周围的配位环境得到高度保持. 此外, 组装的$NaV_2O_2(PO_4)_2F$//$Mg_{0.79}NaTi_2(PO_4)_3$镁离子全电池表现出高的功率和能量密度, 表明$NaV_2O_2(PO_4)_2F$/rGO具有实际应用的潜力. 本工作在MIBs正极材料的工作电压方面实现了突破并为发展高能量密度的MIBs提供了新的机会.